Li1.4Al0.4Ge0.4Ti1.4(PO4)3 promising NASICON-structured glass-ceramic electrolyte for all-solid-state Li-based batteries: Unravelling the effect of diboron trioxide

Journal of the European Ceramic Society 42 (2022) 1023–1032

Contents lists available at ScienceDirect

Journal of the European Ceramic Society

journal homepage: www.elsevier.com/locate/jeurceramsoc

$Li_{1.4}Al_{0.4}Ge_{0.4}Ti_{1.4}(PO_4)_3$ promising NASICON-structured glass-ceramic electrolyte for all-solid-state Li-based batteries: Unravelling the effect of diboron trioxide

Sofia Saffirio [a], Marisa Falco [b,c], Giovanni B. Appetecchi [d], Federico Smeacetto [a,**], Claudio Gerbaldi [b,c,*]

[a] GLANCE Group, Department of Applied Science and Technology (DISAT), Politecnico di Torino, C.so Duca degli Abruzzi 24, 10129, Torino, Italy
[b] GAME Lab, Department of Applied Science and Technology (DISAT), Politecnico di Torino, C.so Duca degli Abruzzi 24, 10129, Torino, Italy
[c] National Reference Center for Electrochemical Energy Storage (GISEL) - INSTM, Via G. Giusti 9, 50121, Firenze, Italy
[d] ENEA, Materials and Physicochemical Processes Technical Unit (SSPT-PROMAS-MATPRO), Via Anguillarese 301, 00123, Rome, Italy

ARTICLE INFO

Keywords:
Lithium battery
Solid electrolyte
Glass ceramic
Single ion conductor
NASICON

ABSTRACT

Li-ion batteries (LIBs) are the ubiquitous technology to power portable electronics; however, for the next-generation of high-performing electrochemical energy storage systems for electric vehicles and smart grid facilities, breakthroughs are needed, particularly in the development of solid-state electrolytes, which may allow for enhanced energy density while enabling lithium metal anodes, combined with unrivalled safety and operative reliability. In this respect, here we present the successful synthesis of a glass-ceramic $Li_{1.4}Al_{0.4}Ge_{0.4}Ti_{1.4}(PO_4)_3$ NASICON-type solid-state electrolyte (SSE) through a melt-casting technique. Being grain boundaries crucial for the total ionic conductivity of SSEs, the effect of the addition of diboron trioxide (B_2O_3, 0.05 wt.%) to promote their liquefaction and restructuring is investigated, along with the effects on the resulting microstructures and ionic conductivities. By the thorough combination of structural-morphological and electrochemical techniques, we demonstrate that bulk materials show improved performance compared to their powder sintered counterpart, achieving remarkable ion mobility (> 0.1 mS cm^{-1} at –10 °C) and anodic oxidation stability (> 4.8 V vs Li^+/Li). The addition of B_2O_3 positively affects the grain cohesion and growth, thus reducing the extension of the grain boundaries (and the related grain/grain interface resistance) and, therefore, increasing the overall ion mobility. In addition, B_2O_3 is seen to contrast the microcracks formation in the LAGTP system under study which, overall, shows very promising prospects as SSE for the next-generation of high-energy density, safe lithium-based batteries.

1. Introduction

The lithium-ion (Li-ion) battery (LIB) is the state-of-the-art device commercially adopted, which empowers our smart electronic and cordless power tools, and, more recently, all-electric, plug-in and hybrid electric vehicles (BEVs, PEVs, PHEVs, etc.). In its standard configuration, LIB uses an insulating separator to keep positive and negative electrodes apart, with a liquid electrolyte solution for alkali metal ions (Li^+) transport, which poses severe safety risks, chiefly in case of battery damage, such as swelling caused by temperature change or leakage caused by external forces, and thermal/electric abuse. In addition, greatly enhanced overall energy density is fundamental, which is not possible by just increasing the number of cells without increasing the unit price and the internal space occupied in vehicles. Actually, top-performing market research agencies and data analytics companies expect that PHEVs/BEVs will replace ICE (internal combustion engine) vehicles in the coming years, to become the mainstream and undisputed choice in transportation industry. The best possible way to have at least close mileage as the current ICE vehicles is to increase the capacity of battery cells. This is exactly the main reason why we need a solid-state

* Corresponding author at: GAME Lab, Department of Applied Science and Technology (DISAT), Politecnico di Torino, C.so Duca degli Abruzzi 24, 10129, Torino, Italy.
** Corresponding author: GLANCE Group, Department of Applied Science and Technology (DISAT), Politecnico di Torino, C.so Duca degli Abruzzi 24, 10129, Torino, Italy.
E-mail addresses: federico.smeacetto@polito.it (F. Smeacetto), claudio.gerbaldi@polito.it (C. Gerbaldi).

https://doi.org/10.1016/j.jeurceramsoc.2021.11.014
Received 29 July 2021; Received in revised form 3 November 2021; Accepted 8 November 2021
Available online 10 November 2021

battery, which is foreseen to provide higher (at least 2–3 times) energy density than standard liquid-electrolyte based LIBs by enabling the use of high operating voltage (high-V) cathodes in combination with lithium metal anodes and avoiding the use of additional components for safety. In addition, it will allow for the use of light modules and packs, thus saving more internal space to increase the amount of active materials. A solid-state battery uses a solid electrolyte, which plays the role of separator as well, thus overcoming the main problems of standard LIBs, *viz.* flammability, resistive SEI at the electrode interface leading to capacity loss, electrolytic decomposition at high anodic potential values limiting the use of high-V cathodes, hazardous thermal runaway and leakage. The scientific community in the field is highly active from several decades and, recently, the use of inorganic solid electrolytes instead of their organic liquid counterpart was demonstrated to improve environmental stability, simplify cell design, increase mechanical strength to suppress lithium dendrite growth [1], increase safety [2], enhance thermal stability and widen the electrochemical stability window. For practical consideration, solid electrolytes are required to possess sufficiently high ionic conductivities, in the order of at least 10^{-4} S cm^{-1} at room temperature [3], as well as good chemical stability and ease of manufacturing [4].

NASICON-structured ceramic electrolytes are among the most attractive solid-state ionic conductors for energy storage devices. In particular, LATP ($Li_{1+x}Al_xTi_{2-x}(PO_4)_3$) and LAGP ($Li_{1+x}Al_xGe_{2-x}(PO_4)_3$) [5] are promising systems for this type of applications [6] and numerous studies were reported in the literature so far [7]. LATP and LAGP are crystalline solid solutions based on the $LiTi_2(PO_4)_3$ and $LiGe_2(PO_4)_3$ systems respectively, in which the tetravalent Ti^{4+} and Ge^{4+} ions are partially substituted by the trivalent Al^{3+} ions [8]. Additional Li^+ ions are encompassed in the solutions to restore the charge neutrality of the systems [2]. LATP and LAGP crystallize in a rhombohedral lattice consisting of PO_4 tetrahedra sharing corners with TiO_6 and GeO_6 octahedra that give rise to a three-dimensional pathway [9], enabling for lithium-ion conductivity.

The partial substitution of Ge^{4+} for Ti^{4+}, resulting in the LAGTP system, was first proposed by Xu et al. [4] for the preparation of melt-quenched glass-ceramics of $Li_{1.4}Al_{0.4}(Ge_{1-x}Ti_x)_{1.6}(PO_4)_3$ (x = 0÷1.0) showing an overall ionic conductivity of 6.2×10^{-4} S cm^{-1} at room temperature when x = 0.33, after having been treated at 950 °C for 18 h. The idea was to combine the higher lithium ion conductivity of LATP with the better chemical stability of LAGP, being Ge^{4+} presumed to be a more stable host compound than Ti^{4+} for Li^+ ion mobility. Li^+ ions are in fact inserted into the solid solution upon the $Al^{3+}\rightarrow Ge^{4+}$, Ti^{4+} substitutions, and LAGP showed a higher solubility limit of aluminium than LATP [10,11].

Being the LATP glass system difficult to obtain by a glass-ceramic route [2], this processing method was mainly investigated for LAGP systems [10,12–16], while little attention was paid to the use of this technique for the fabrication of LAGTP systems. Solid-state and sol-gel synthesis routes were largely used instead. Maldonado-Manso et al. [17], for instance, reported ionic conductivities ranging between 2 and 7 $\times 10^{-4}$ S cm^{-1} at room temperature for the $Li_{1+x}Al_xGe_yTi_{2-x-y}(PO_4)_3$ ($0.20 \leq x \leq 0.8$, y = 0.8, 1.0) system. The powders were obtained through solid-state reaction and sintered at 950 °C for 12 h. The same synthesis was used by Šalkus et al. [18] to investigate LAGTP compounds with x = 0.1÷0.3 and y = 0.07÷0.21, demonstrating that the $Al^{3+}\rightarrow Ge^{4+}$,$Ti^{4+}$ substitutions increase lattice parameters and Li-ion conductivities in active material grains, yielding an overall conductivity of about 3.2×10^{-3} S cm^{-1} at 600 K when x = 0.3 and y = 0.21, after sintering at 1363 K for 1 h. $Li_{1.4}Al_{0.4}Ti_{1.6-x}Ge_x(PO_4)_3$ (x = 0 ÷ 1.0) compounds were synthesized by Zhang et al. [19] with precursors prepared using the sol-gel method. The highest total lithium-ion conductivity for the pellets, sintered at 950 °C for 11 h, was found to be about 1.3×10^{-3} S cm^{-1} at room temperature when x = 0.2.

Regardless of the type of method adopted for the synthesis of powders, either solid-state or sol-gel, the sintering route brings along intrinsic densification limits and, despite the possibility to promote densification by decreasing the particle size and by narrowing its distribution [20], reduced interparticle contact is responsible for ineffective ion transport among grains [2], as voids reduce the effective cross-section of a sample [6], thus affecting the overall conductivity of solid electrolytes. Given the possibility to evaluate the intrinsic conductivity of a material through the use of correction equations, such as Bruggeman's [21] or Archi's law [22] that consider the volume fraction of pores in a sample, the presence of pores still remains disadvantageous when the material is used as a ceramic electrolyte to assemble an all-solid-state battery. For this reason, the use of dense bulk components in the place of sintered materials could help overcoming these limits, also widening the spectrum of possible final forms and sizes [4] and allowing for microstructural control [2].

Along with the presence of pores, grain boundaries [6] and microcracks [20] were reported to strongly affect the ionic conductivity of NASICON-type materials. In particular, Martens et al. [9] proved that the overall ionic conductivity is mostly determined by the ion transport process occurring at the grain/grain interface, and suggested that improved ionic conductivities could be achieved by increasing the geometric ratio of grain size to grain boundary width *D/d*. Similarly, Jackman et al. [23] gave evidence that improvements in grain boundary conductivity were due to a reduction in void spaces, through which lithium ion mobility is hindered, and not to an increase in the actual conductivity of the material located at the grain/grain interface. According to the same authors, microcracking was also demonstrated to negatively affect the ionic conductivity.

In this work, the microstructure, ionic conductivity and electrochemical properties resulting from both powder sintering and bulk heat treatment of mixed LAGTP glass-ceramic electrolytes are investigated, with the aim to demonstrate the enhanced performances of a bulk material with respect to its sintered counterpart for a given composition. In particular, following the work by Zhang et al. [19], who exploited a sol-gel method, the $Li_{1.4}Al_{0.4}Ge_{0.4}Ti_{1.4}(PO_4)_3$ system is here synthesized through the melt-casting technique. The effect of the addition of diboron trioxide (B_2O_3, 0.05 %wt) to enhance sintering, as for the LAGP system melt-quenched by Jadhav et al. [24] and synthesized by Kim et al. through sol-gel [25], is also investigated. Indeed, thanks to its melting temperature of about 450 °C, B_2O_3 was reported to promote the liquefaction of grain boundaries during the heat treatment and, being grain boundaries crucial for the overall ionic conductivity, its addition should positively affect grain cohesion and growth, thus reducing the extension of the grain boundaries and increasing the ion mobility, while also contrasting the microcracks formation.

2. Materials and methods

2.1. Synthesis of the NASICON-structured glass ceramics

The NASICON-structured glass ceramics were prepared using a melt-quenching route. Stoichiometric amounts of Li_2CO_3 (EMSURE ACS, 99.0 %), Al_2O_3 (Alfa Aesar, 99.9 %), GeO_2 (Aldrich, 99.99 %), TiO_2 (Panreac, 99.0 %), $NH_4H_2PO_4$ (Carlo Erba, 99.9 %) were used as precursors for the preparation of the mixed Ge/Ti glass ceramic with composition $Li_{1.4}Al_{0.4}Ge_{0.4}Ti_{1.4}(PO_4)_3$, consisting in $17.5Li_2O$-$5Al_2O_3$-$5GeO_2$-$35TiO_2$-$37.5P_2O_5$ (mol.%), namely LAGTP. Additionally, H_3BO_3 (Sigma-Aldrich, 99.5 %) was used for the preparation of the B_2O_3-doped glass ceramic with composition $Li_{1.4}Al_{0.4}Ge_{0.4}Ti_{1.4}(PO_4)_3$ + 0.05 %wt B_2O_3, namely LAGTPB.

The precursors were thoroughly mixed for 24 h and heated up to 350 °C in an Al_2O_3 crucible at a heating rate of 10 °C min^{-1} and held at that temperature for 30 min to release the ammonia coming from $NH_4H_2PO_4$. A further isothermal step at 700 °C for 30 min was performed to release the carbon dioxide. Ultimately, the powders were heated up to 1450 °C for 1 h to allow the formation of a homogeneous melt. The resulting LAGTP and LAGTPB glasses were casted onto a brass plate at room

temperature and immediately transferred into a furnace at 550 °C for 2 h to relieve thermal stresses. After that, two different routes were investigated: the powder sintering route and the heat treatment route of the bulk glass. In the former case, LAGTP and LAGTPB powders were obtained by use of a single 50 mm ball in a zirconia vibratory ball mill (Fritsch, Pulverisette 0) for 2 h, sieved under 25 μm and pressed into pellets (13 mm in diameter), which were sintered to yield LAGTP-s and LAGTPB-s samples, respectively. In the second case, LAGTP and LAGTPB were heat-treated in their bulk form resulting in LAGTP-b and LAGTPB-b. Both powder sintering and bulk heat-treatments were carried out at 950 °C for 10 h, following the results of differential thermal analysis detailed in paragraph 3.1.

2.2. Characterization techniques

Characteristics temperatures, such as glass transition (T_g), onset crystallization (T_x) and peak crystallization (T_p) temperatures of the glass-ceramic materials in the form of powders were evaluated by differential thermal analysis (DTA, Netzsch, DTA 404 PC) in the temperature range between 25 and 1100 °C at a heating rate of 10 °C min^{-1} in synthetic air. The sintering behavior of powders was also followed by means of hot stage microscopy (HSM, Hesse Instruments, Heating microscope EM301) from 25 to 1100 °C at a scan rate of 10 °C min^{-1}. Based on the DTA and HSM data, different heat treatments were carried out for the LAGTP and LAGTPB systems.

Crystalline phases were identified by X-Ray diffraction analysis (XRD, Panalytical, Xpert3 MRD) at RT using Cu Kα radiation at a voltage of 40 kV and a current of 40 mA. The XRD patterns were recorded in the 2θ range of 10−70 °. The relative density *d* was derived from experimental Archimedes evaluations according to Eq. 1:

$$d = (w_a\text{-}w_w)d_w/w_a \quad (1)$$

where w_a and w_w are the weight of the sample evaluated in air and in water, respectively, d_w is the density of water and *d* the resulting density of the glass-ceramic component [3].

Microstructures of the glass-ceramics were observed by means of scanning electron microscopy (SEM, Jeol, JCM-6000Plus, BenchtopSEM provided with an Everhart Thornley type SE detector and a high sensitivity solid state BSE detector) on the as-treated, polished and fracture surfaces of each sample, under high vacuum and at a voltage of 15 kV. Elemental analysis was performed through energy-dispersive X-ray spectroscopy (EDS, Jeol, EX-37,001) in the same operating conditions.

Polished samples were Au sputtered on both sides and served for ionic conductivity measurements. The Au-coated solid electrolytes were sandwiched between two stainless-steel (SS) ion-blocking electrodes in SS/electrolyte/SS configuration of an EL-Cell Std (EL-CELL, Germany) electrochemical test cell. The ionic conductivity was evaluated by electrochemical impedance spectroscopy (EIS) using a VMP3 potentiostat/galvanostat (Biologic) with an oscillating potential of 20 mV in the frequency range between 300 kHz and 1 Hz. The test was carried out between -20 and 80 °C using an environmentally controlled climate chamber (MK 53 E2 from BINDER, Germany). The cells were kept for 100 min at each temperature with intervals of 10 °C for proper equilibration. The Nyquist plots were analysed using Ec-Lab software (V 10.44). The ionic conductivity (σ_i) values were determined according to Eq. 2:

$$\sigma_i = t/AR \quad (2)$$

where *t* is the sample thickness, *A* is the area of the electrodes and *R* is the total resistance [2].

The activation energies (E_a) for Li^+ ion diffusion were extracted from the linear fit of the ionic conductivity data *versus* the reciprocal of temperature (*T*) in the Arrhenius plot, according to Eq. 3:

$$\ln\sigma = \ln a - (E_a/RT) \quad (3)$$

where *a* is the pre-exponential factor and *R* is the universal gas constant [1].

The DC resistance (R_{DC}) of the samples was measured recording the current response (*I*) of symmetric SS/electrolyte/SS cells with ion-blocking electrodes at a fixed voltage (*E*) of 2 V applied for 900 s at 25 °C. A voltage of 3 V was applied in one case to obtain a clear current response. The electronic conductivity (σ_e) was calculated as follows (Eq. 4) [6]:

$$\sigma_e = t\ I\ /(A\ E) = t\ /(A\ R_{DC}) \quad (4)$$

The electrochemical stability window (ESW) of the most conductive samples was evaluated using in-house made T-cells in a three electrodes configuration with Li metal disks as both quasi reference (QRE) and counter (CE) electrodes, and LAGTP-b or LAGTPB-b based composite as the working electrode (WE). The composite electrodes were prepared by a standard method from NMP (N-methyl pyrrolidone, Merk) slurry containing LAGTPB-b (75 wt.%), conductive carbon (C65, Imerys, 15 wt.%) and PVdF (Solef 6020, Solvay, 10 wt.%). The slurry was deposited onto an Al foil or Cu foil, dried overnight at ambient temperature, cut into disks (with a 10 mm diameter) and vacuum dried at 120 °C for 1 day prior use to remove water and residual NMP solvent traces. The resulting composite electrodes had a mass loading of 2.0 mg cm^{-2}. For comparison purpose, carbon-coated Al (CC-Al) or Cu (CC-Cu) electrodes were prepared by the same method, from a slurry containing C65 (90 wt.%) and PVdF (10 wt.%). Three Whatman glass fiber disks (with a diameter of 10 mm, ≈ 120 μm thick) were used as separators and drenched in different liquid electrolytes. Battery grade LP30 (Solvionic, France), consisting in 1 M $LiPF_6$ in EC:DMC (1:1 v/v) was used as the electrolyte for the determination of the anodic stability window (ASW). An ether-based electrolyte consisting in lithium bis(trifluoromethansulfonyl) imide (LiTFSI) 1 m in tetraethylene glycol dimethyl ether (G4), battery grade from Solvionic (France), was used for the evaluation of the cathodic stability window (CSW). The cyclic voltammetry (CV) tests were carried out at ambient temperature (≈ 23 °C) at a scan rate of 0.1 mV s^{-1} using a VMP3 potentiostat/galvanostat (Biologic) in the range 0.1–3 V (CSW) or 3–5 V (ASW). The electrodes coated on Cu and Al were used as the WEs for the determination of the CSW and the ASW, respectively.

For an additional test to determine the ASW of LAGTPB-b, a multilayered cell was prepared using a crosslinked poly(ethylene oxide) (PEO)-based polymer electrolyte (PEO-G4) as an interlayer between Li metal and the thermally treated bulk ceramic LAGTPB-b. The PEO-G4 film was prepared by a solvent-free procedure consisting in hot-pressing followed by UV-induced crosslinking starting from a mixture containing equal amounts of PEO (200 kDa, Merck) and G4 (38.75 wt %), LiTFSI (15 wt%) and benzophenone (15 wt%, from Merck) photo-initiator as detailed elsewhere [26]. This method was adopted to avoid the reduction of LAGTPB-b in contact with Li metal. The Au WE was directly sputtered on ceramic LAGTPB-b, yielding a two-electrode cell in the configuration Li/PEO-G4/LAGTPB-b/Au. The Li metal foil was used as both the counter and the reference electrodes for the CV measurement up to 5.5 V at 0.1 mV s^{-1}.

3. Results and discussion

3.1. Thermal characterization

DTA measurements (Fig. 1) were carried out on the powders of LAGTP and LAGTPB to determine their glass transition (T_g), onset crystallization (T_x) and peak crystallization (T_p) temperatures, which are listed in Table 1.

No crystallization peak was detected for both LAGTP and LAGTPB, which directly crystallized onto the brass plate during casting. From a kinetic point of view, this is likely ascribed to the cooling rate undergone by glasses when poured onto a plate in air being lower than their

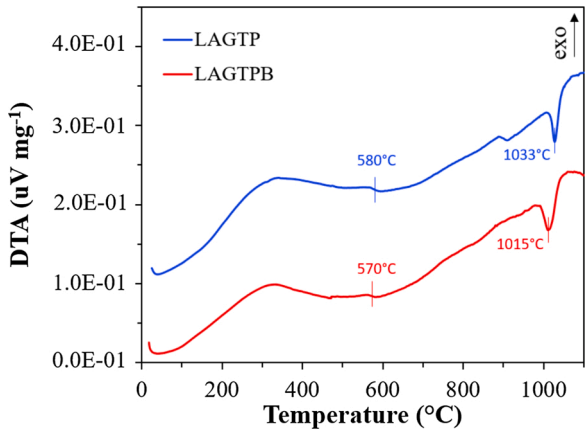

Fig. 1. DTA curves of as-casted LAGTP and LAGTPB.

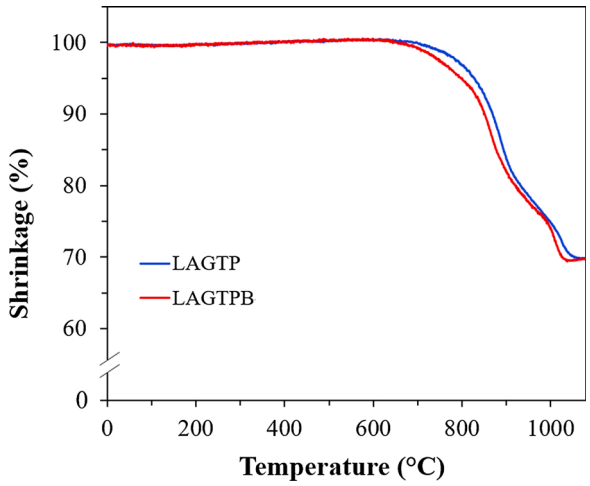

Fig. 2. HSM curves of as-casted LAGTP and LAGTPB upon a scanning rate of 10 °C min^{-1}.

Table 1
Characteristic temperatures (T_g, T_x, T_p) and shrinkage behavior (T_{FS}, shrink.% at 950 °C) evaluated through DTA and HSM for as-casted LAGTP and LAGTPB.

	T_g (°C)	T_x (°C)	T_p (°C)	T_{fs} (°C)	Shrink.% at 950 °C
LAGTP	580	ND	ND	780	19 %
LAGTPB	570	ND	ND	770	21 %

intrinsic crystallization rate. Despite the absence of crystallization peaks, the T_g values were identified at 580 and 570 °C for LAGTP and LAGTPB respectively, presumably due to very small amounts (too low to be detected) of LAGTP conductive phase that could not completely crystallize during casting. This hypothesis is supported by the analogous absence of T_g and T_m (melting) corresponding to the amorphous B_2O_3 contained in LAGTPB, which should have been visible at 278 and 450 °C, respectively, according to the literature [27,28]. Indeed, none of them was detected, being the amount of B_2O_3 as low as 0.05 %.wt of the overall glass composition. Nevertheless, such a low amount was enough to decrease the value of T_g by 10 °C for LAGTPB-p, where B_2O_3 acted as a sintering aid.

A low-intensity endothermic peak was also detected, namely at 1033 and 1015 °C for LAGTP and LAGTPB, respectively. GeO_2 was largely reported [13,29,30] to appear as a secondary phase in LAGP systems. This oxide shows a dimorphic transformation from its low temperature rutile-like tetragonal (P42/mnm) structure to its high-temperature α-quartz-like (P3221) trigonal (hexagonal) structure at 1033 °C [31, 32]. As a consequence, the endothermic transformations registered through DTA could be attributed to the presence of this secondary phase in our LAGTP and LAGTPB systems. Nevertheless, due to the shift registered for LAGTPB, the peak of which was anticipated to 1015 °C, this hypothesis should be further investigated.

HSM evaluations carried out on LAGTP and LAGTPB powders sieved under 25 μm revealed different shrinkage behaviors (Fig. 2). The first shrinkage temperature (T_{FS}, considered as the temperature at which the sample was shrunk to 97 % of its initial dimension) and the shrinkage percentage at 950 °C were evaluated. Results are listed in Table 1.

The shrinkage percentages are an important parameter for the extent of densification at the sintering temperature at 950 °C. In particular, 19 and 21 % shrinkage percentages were detected at 950 °C for LAGTP and LAGTPB, respectively. Both LAGTP and LAGTPB showed a continuous shrinkage behavior, resulting in T_{FS} equal to 780 and 770 °C, respectively, which highlights the influence of B_2O_3 on the first shrinkage temperature. The early shrinkage of pellets upon addition of 0.05 %wt B_2O_3 is the most interesting and significant result.

Based on the DTA and HSM results, specific heat treatments were targeted for LAGTP and LAGTPB in their bulk and sintered forms. An upper temperature of 950 °C was set for all the samples to achieve the maximum densification of sintered powders and, at the same time, to promote grain growth of both sintered and bulk samples, while limiting the lithium loss and the microcracking occurring at high temperature. Indeed, lithium in the form of Li_2O was reported by Waetzig et al. [20] to vaporize above 950 °C leading to the partial transition of LATP into non-conductive secondary phases, such as $AlPO_4$, that could exhibit microcracks due to the resulting lattice shrinkage. The same authors also proved that the high thermal expansion anisotropy of the LATP lattices is responsible for the formation of microcracks across the main conductive phase at temperatures above 1000 °C. The same behavior can be extended to LAGP and, thus, to LAGTP. Based on these considerations and the HSM results discussed above, a single 10 h sintering treatment at 950 °C was set for LAGTP and LAGTPB to yield sintered LAGTP-s and LAGTPB-s, respectively. Analogously, bulks were heat treated at 950 °C for 10 h and LAGTP-b and LAGTPB-b were obtained.

Density values obtained through Archimedes method (see eq. 1 in paragraph 2.2) for the sintered and heat-treated samples are compared in Table 2, demonstrating the improved densification of bulk samples compared to their sintered counterparts, but also confirming the positive effect of B_2O_3 on the shrinkage behavior of powders, as previously assessed by the HSM experiments.

According to the results listed in Table 2, decreasing relative density values of 95.6 %, 95.2 %, 92.5 % and 92.2 % were obtained for LAGTPB-p, LAGTP-p, LAGTPB-s and LAGTP-s, respectively, referring to the theoretical density value of 2.95 g cm^{-3} reported in the literature [46] for the $LiTi_2(PO_4)_3$ NASICON-type structure.

3.2. Crystalline phase analysis

XRD spectra were recorded for LAGTP and LAGTPB in their as-casted form, as well as after their sintering and bulk heat treatment at 950 °C for 10 h. Resulting diffraction patterns are shown in **Fig. S1** and Fig.3, respectively; the reflections for each of the corresponding crystalline phases are indicated above the diffraction peaks. The conductive crystalline phase $LiTi_2(PO_4)_3$ (JCPDS reference code: 00−035-0754; major reflections at 24.492 °, 20.844 ° and 29.642 °) was identified for all samples. $AlPO_4$ (JCPDS reference code: 01−072-1161; major reflections

Table 2
Density values obtained through Archimedes method for LAGTP and LAGTPB samples, either sintered (LAGTP-s and LAGTPB-s) or bulk heat-treated (LAGTP-b and LAGTPB-b).

	LAGTP-s	LAGTPB-s	LAGTP-b	LAGTPB-b
Density (g cm^{-3})	2.72	2.73	2.81	2.82

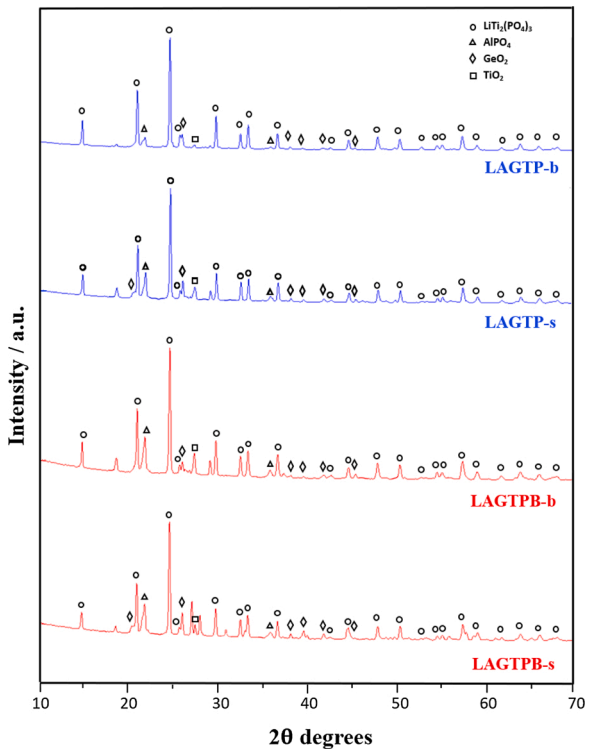

Fig. 3. XRD spectra of LAGTP and LAGTPB after powder sintering (-s) or bulk heat treatment (-b). The XRD patterns were recorded in the 2θ range of 10-70 ° at a voltage of 40 kV and a current of 40 mA.

at 21.763 °, 35.746 ° and 31.108 °), GeO_2 (JCPDS reference code: 01−083-2474; major reflections at 25.961 °, 20.556 ° and 38.058 °) and TiO_2 (JCPDS reference code: 01−088-1172; major reflections at 27.606 °, 54.631 ° and 36.242 °) secondary insulating phases were also detected for both samples.

The increased presence of secondary phases across the different samples could be either identified through an increase in the relative intensity of a given peak or to the appearance of new peaks corresponding to the same crystalline phases. In this regard, one should consider that the second principal peak of GeO_2, located at 20.556 °, is overimposed to the second $LiTi_2(PO_4)_3$ peak at 20.844 °, being more intense in most of the cases. Only by sintering the samples at 950 °C for 10 h, this peak was sufficiently intense to be detected and clearly distinguished in LAGTP-s and LAGTPB-s.

The presence of secondary phases was found to increase in sintered samples, compared to the bulk heat-treated ones for a given composition (i.e., LAGTP-s and LAGTP-b, or LAGTPB-s and LAGTPB-b). Diffraction patterns of the as-casted materials are shown in **Fig. S1** to visualize this different increase. In fact, as both the -s and -b samples derive from the same as-casted material (LAGTP-p or LAGTPB-p), they possess the same initial amount of secondary phases.

However, the milling step brings along the grinding and dispersion of these initial phases, resulting in a more widespread formation of secondary phases that are likely to grow at high temperatures across the powder-sintered pellets. For a given composition, this growth is likely due to the increased specific surface area of the particles compared to the bulk materials. Further investigations should be carried out to evaluate the presence of secondary phases at the grain boundary or in the pores of the sintered samples, and to evaluate a possible surface-driven crystallization mechanism for these systems. This effect would also be responsible for the increased amount of unassigned reflections ascribed to non-identified secondary phases in sintered samples. Analogously, the presence of secondary phases was found to increase in the presence of B_2O_3 for a given synthesizing route, presumably due to the microstructural reorganization induced by the addition of this sintering aid showing a melting temperature of about 450 °C [24].

As a result, LAGTP-b is expected to show the most promising ion conducting behavior, followed by LAGTPB-b and by the sintered materials. However, microstructure is also expected to play a fundamental role on the final ionic conductivity values, as discussed in the next paragraph 3.3.

Overall, a 0.25 ° shift of the diffraction peak positions towards lower angles compared to the reference diffraction pattern of $LiTi_2(PO_4)_3$ was observed in all samples. This shift indicates the changes in lattice parameters induced by replacement of Ti^{4+} with $Ge^{4+}$and Al^{3+}, proving the formation of LAGTP solid solutions.

3.3. Microstructural analysis

SEM micrographs of the non-polished, fracture and polished surfaces are shown in Fig. 4 upon detection of secondary electrons (SEs). The effects of the addition of B_2O_3 and of the different synthesizing routes, either sintering or bulk heat-treatment, are here clearly visible. Considering sintered LAGTP-s and LAGTPB-s, both treated at 950 °C for 10 h, the formation of larger cohesive grains was in fact observed in the latter, as evidenced by its non-polished surface. A similar trend was registered for bulk heat-treated LAGTP-b and LAGTPB-b, the latter being characterised by the formation of larger elongated grains and cohesive grain boundaries. The improved grain size and cohesion observed in both cases could be attributed to the presence of amorphous B_2O_3, which melts at about 450 °C promoting the liquefaction of grain boundaries [24] and, thus, the rearrangement and growth [25] of grains during the sintering or heat-treatment process itself. Thanks to this liquefaction, the formation of microcracks in LAGTPB-s and LAGTPB-b was observed to be remarkably reduced in comparison to LAGTP-s and LAGTP-b, respectively.

A further investigation was carried out on sintered LAGTPB-s through EDS semi-quantitative analysis to shed light on the composition of the white areas observed in sintered samples. Results are shown in Fig. 5 and highlight the presence of bright Ge-rich regions, with an amount of Ge as high as 17.79 %at, which could not instead be at all detected in the darker Ge-poor surrounding region. As a consequence, they could be attributed to the formation of GeO_2 secondary phase. These results are in good agreement with the XRD results previously discussed in paragraph 3.2, which showed that secondary phases are more likely to form in powder sintered samples.

As regards the effect of the two different synthesizing routes, bulk materials showed enhanced densification, grain size and grain cohesion compared to their sintered counterparts. In accordance with HSM results and density values derived through Archimedes method (Table 1 and Table 2, paragraph 3.1), the presence of intergranular voids was in fact reduced in LAGTP-b and LAGTPB-b bulk samples. As a matter of fact, micrographs of the polished surfaces highlighted the presence of few localized voids of the order of about 5 μm in the bulk LAGTP-b and LAGTPB-b samples, which instead appeared narrower in size but more widespread through the sintered LAGTP-s and LAGTPB-s. Despite the avoidance of sintering, the presence of voids in the bulk materials is likely ascribed to the casting procedure and to the temperature gradient induced by cooling on the brass plate. Intergranular voids observed in the sintered samples are instead ascribable to the sintering process.

Along with the increased densification of the materials, the bulk route also positively affected the resulting microstructures, giving rise to better-defined grains particularly visible from the fracture surfaces. Such microstructures are expected to be the most promising in terms of ionic conductivity, thanks to their improved grain size and cohesion. For this reason, the fracture surfaces of LAGTP-b and LAGTPB-b were further investigated by use of a FESEM microscope. Micrographs are shown in Fig. 6. Evidence of the effect of B_2O_3 on the resulting grain size at a given magnification was given. In particular, larger grains with an average size of 2 μm were observed all across LAGTPB-b, while smaller grains (1 μm),

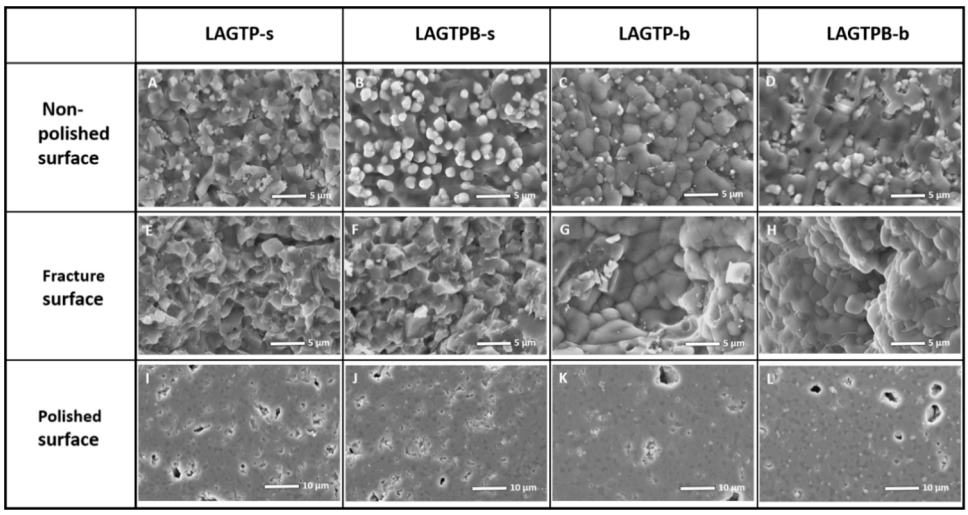

Fig. 4. SEM micrographs of non-polished, fracture and polished surfaces of sintered and bulk heat-treated LAGTP and LAGTPB. From above: sintered LAGTP-s (A,E,I) and LAGTPB-s (B,F,J), bulk heat treated LAGTP-b (C,G,K) and LAGTPB-b (D,H,L). From the left: non-polished (A,B,C,D), fracture (E,F,G,H) and polished (I,J,K, L) surfaces.

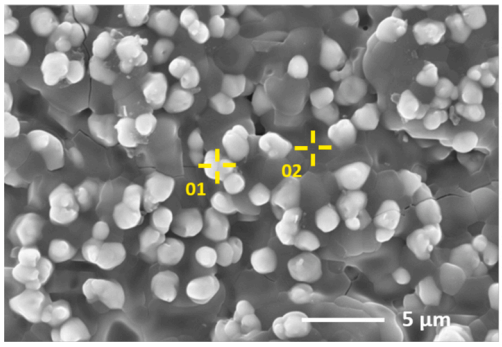

01

Element	Atomic %
Li	ND
B	ND
O	75.03
Al	3.23
P	2.90
Ti	105
Ge	**17.79**

02

Element	Atomic %
Li	ND
B	ND
O	58.10
Al	4.49
P	17.33
Ti	20.08
Ge	**ND**

Fig. 5. EDS analysis performed on powder sintered LAGTPB (LAGTPB-s) to evaluate the composition of the bright areas observed on its non-polished surface. The analysis was carried out in high vacuum and at a voltage of 15 kV.

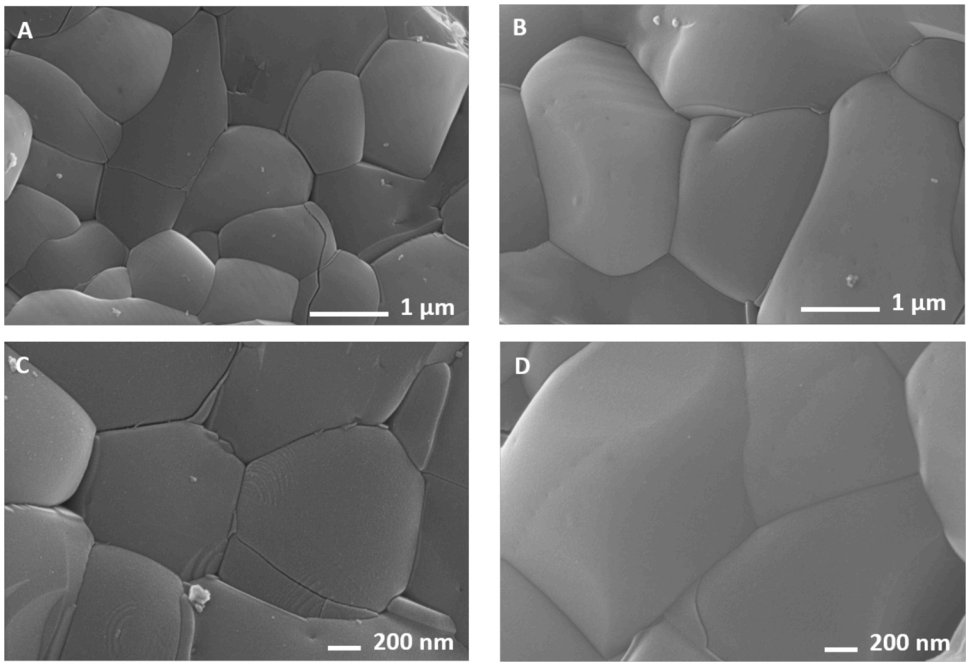

Fig. 6. FESEM micrographs of the fracture surfaces of bulk heat-treated LAGTP-b (A and C) and LAGTPB-b (B and D). Samples were treated at 950 °C for 10 h.

among few larger grains, were found in LAGTP-b. Both inter and intragranular microcracks were diffusively present in LAGTP-b. On the contrary, no microcrack formation was observed for LAGTPB-b, which resulted in highly cohesive grains.

According to the SEM microstructures discussed above and in contrast with the XRD results, the bulk heat-treated LAGTPB-b is expected to possess the highest lithium ion conductivity among all samples, followed by LAGTP-b and by the powder-sintered pellets.

3.4. Ionic conductivity and electrochemical characterization

In view of their possible application as separating electrolytes in all-solid-state Li-based batteries, the as sintered glass-ceramics were characterised by EIS in terms of ionic conductivity at varying temperatures, lithium ion transference number, and further tested in terms of electrochemical stability window.

Fig. 7**A** shows the Nyquist plot of representative EIS spectra for the sintered and heat-treated bulk samples collected at 20 °C in symmetric SS/electrolyte/SS cells. In the case of the more resistive sample (i.e., LAGTPB-s), the spectra consist in a high frequency semi-circle, which does not intercept the axes origin, coupled with a straight line at low frequencies.

These spectra were fit using the equivalent circuit shown in the inset of Fig. 7A (top). Constant phase elements (Q) were used in the place of capacitive elements to fit slightly depressed semi-circles at high frequencies and straight lines with different inclinations at low frequencies. These latter arise from charges accumulation at the ion-blocking electrode/electrolyte interface, and are represented by Q2 (capacitive contribution at electrolyte/electrode interface). The parallel combination of R2 and Q1 accounts for the high frequency semi-circle, where R2 and Q1 are attributed to the grain boundary resistance and capacitance, respectively. The element R1 represents the electrolyte bulk resistance, related to the distance from the high frequency intercept with the real axis to the origin of the axes. Therefore, the overall ionic resistance was calculated as the sum of R1 and R2. It is interesting to note how the grain boundary contribution (well pronounced in the LAGTPB-s and LAGTP-s samples) is rather reduced in LAGTP-s and even negligible in LAGTPB-b and LAGTP-b, suggesting a remarkable improvement of the grain-grain interfacial contact, leading to higher ion conduction values. For the less resistive samples (i.e., LAGTP-b, LAGTPB-p, and in some cases for other samples at high temperature), the AC responses consist in an inclined straight line making a non-zero high-frequency intercept. In these cases, the spectra were fitted as the series combination of R3 (overall resistance) and Q2 (inset in Fig. 7A, bottom). The measurement of the electronic conductivity by a DC method (**Fig S2**) confirmed that the material is a pure ionic conductor, being σ_e negligible (in the order of 10^{-8}-10^{-10} S cm^{-1} as shown in Table 4), which results in ionic transference numbers $\geq$ 0.9999. It is worth mentioning here that in order to obtain a clear current output, a relatively high DC voltage of 2 V (in one case 3 V) had to be applied to the cells, below which the current would fluctuate around zero with positive and negative values. Under this condition, the degradation of the electrolyte might have played a role in determining the current flow.

The overall ionic conductivity values are shown in the Arrhenius plot of Fig. 7B. Consistent linear fit ($R^2 > 0.999$) was obtained is all cases. The activation energies are in the range of 0.27−0.35 eV (Table 3), in good agreement with those reported in the literature for similar systems [7,10,4,18]. Notably, the most ionically conducting sample LAGTPB-b shows total ionic conductivity of 0.39 and 0.10 mS cm^{-1} at +20 and -10 °C, respectively. The former is among the highest values reported in the relevant literature [7–10], while the latter satisfies the ionic conductivity targets for solid-state ceramic electrolytes of the H2020 European (EU) Si-DRIVE project (https://sidrive2020.eu/). Research in Si-DRIVE is focused on the development of novel materials to achieve next generation LIBs able to meet the future demands and EU market opportunities, delivering on the challenge of safer, higher energy density and durable LIB chemistries for future BEVs with practical battery operation even at sub-zero temperatures.

The ionic conductivity values of the different samples are strongly affected by the synthesis process, and consequent thermal treatments, which play a role on the microstructure as detailed in paragraphs 3.1−3.4. The highest ionic conductivity is obtained for the samples thermally treated in the bulk form (LAGTP-b and LAGTPB-b), resulting in large grains dimension, with improved cohesion and few localized intergranular voids (Fig. 4). This is also reflected by the absence of distinct signals due to the grain boundaries contribution in the impedance spectra, in the whole range of the investigated temperatures (Fig. 7A). In this respect, the highest σ_i values obtained in this work can be attributed to the positive effect of B_2O_3 promoting grain growth and cohesion. It can be thus concluded that these factors exert a greater positive impact on the final ionic conductivity than the negative undesired impact of the B_2O_3-induced formation of secondary phases detected by XRD analysis. In this regard, Duluard et al. [32] found that small amounts of non-conductive secondary phases, such as $AlPO_4$, can induce a densifying effect which is beneficial for the ionic conductivity, if their unit cell is smaller compared to that of the main conductive phase. Poor σ_i values are observed for the sintered LAGTPB-s sample. In this case, despite the larger grain size, the milling step leads to the widespread distribution of comparatively high amount of insulating secondary

Table 3
Summary of the transport properties extracted from the electrochemical characterization.

Sample	σ_e @ 25 °C (D.C. V) S cm^{-1} (V)	σ_i @ -10 °C S cm^{-1}	σ_i @ 20 °C S cm^{-1}	E_a kJ mol^{-1} (eV)
LAGTPB-b	1.35 10^{-9} (3.0)	1.01 10^{-4}	3.90 10^{-4}	27.40 (0.28)
LAGTPB-s	2.70 10^{-9} (2.0)	4.75 10^{-6}	2.38 10^{-5}	34.19 (0.35)
LAGTP-b	2.06 10^{-10} (2.0)	4.80 10^{-5}	1.81 10^{-4}	29.08 (0.30)
LAGTP-s	3.58 10^{-10} (2.0)	1.92 10^{-5}	9.40 10^{-5}	33.17 (0.34)

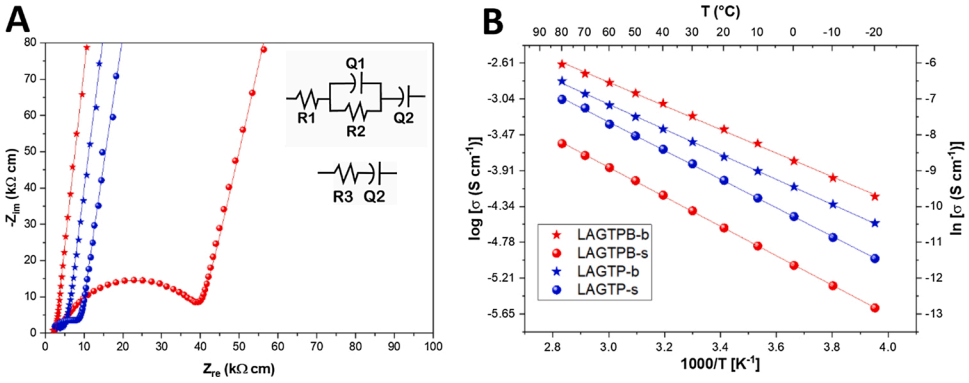

Fig. 7. Nyquist plot of the impedance spectra of symmetric SS/electrolyte/SS cells at 20 °C. (A) The real and imaginary parts of each impedance spectrum were multiplied by the sample area and divided by its thickness to allow for direct comparison. The inset shows the equivalent circuits used to fit the spectra. Ionic conductivity data plotted *vs.* 1000/T of the solid ceramic electrolytes under study (B). Legend of samples is representative for both the plots. Symbols stand for experimental data, straight lines for the fitting curves.

phases, such as GeO_2, $AlPO_4$ and TiO_2 (paragraphs 3.2, 3.3 and Fig. 7), with respect to the other samples, which is most probably responsible for the low conductivity observed. Differently, sintered LAGTP-s shows intermediate σ_i values. The decrease of ionic conductivity with respect to its bulk counterpart LAGTP-b is attributed to the presence of widespread intergranular voids arising from the milling and sintering process, which affect density (see Table 2 and paragraph 3.3). Overall, the ionic conductivity is larger in LAGTPB-b, with large cohesive grains and few localized voids, and it decreases for sintered samples with abundant widespread insulating domains, such as pores, cavities and secondary phases.

Besides the ionic conductivity, the stability of an electrolyte in the voltage window at which the electrodes operate inside an electrochemical cell is a fundamental parameter, particularly for practical battery application. In the Si-DRIVE project, the requirements in this respect are rather demanding; actually, the cells are conceived to work with high energy density silicon-based anodes [33], and Co-free high voltage cathodes operating up to 4.8 V vs. Li^+/Li [34]. To assess the electrochemical stability in the range of interest, the most conductive samples LAGTP-b and LAGTPB-b were used as the WE and evaluated by cyclic voltammetry exploiting in house made T-cells assembled in three electrodes configurations with Li metal disks as QRE and CE electrodes, as detailed in experimental (paragraph 2.2). The as-synthesised materials were milled and processed into composite electrodes containing C65 carbon as electronic conducting additive.

This method was purposely used because the flat surface of the ceramic bulk could limit the reaction area, leading to a low current output during the CV. Also, carbon-rich WEs allow to satisfactorily simulate the behaviour of a practical device, leading to much more reliable results than those obtained using inert WEs (steel, nickel, platinum). Indeed, misleading experimental electrochemical stability windows were previously reported for ceramic Li-ion conductors, largely exceeding the calculated thermodynamic stability limits [35]. Additionally, it allows test cells assembly using Li metal as the reference electrode, thus avoiding conversion errors and giving reliable information directly related to the operative voltages of the electrodes in real cell configuration. Indeed, NASICON-type ceramic conductors are well known to be unstable in contact with Li metal, due to the reduction of Ti^{4+} and Ge^{4+}, leading to the formation of a mixed ionic and electronic conductive interface [36].

Fig. 8**A** shows the CV in the range 3 – 0.1 V vs. Li QRE using LAGTPB-b composite WE (the CV for non B_2O_3-doped LAGTP-b is shown in the supporting information, **Fig. S3**). The voltage range investigated was not further extended cathodically to avoid lithium plating. The measurement was carried out in a three electrodes cell assembly using LiTFSI 1 m in G4 as the electrolyte (see details in experimental), which was selected due to the good stability of ethers at low voltage vs. Li^+/Li [37,38]. A small signal reduction at about 2.4 V vs. Li QRE can be detected during the first cathodic sweep. This is attributed to the redox reaction $Ti^{4+} + e^- \rightarrow Ti^{3+}$ and consequent Li^+ insertion, based on data reported for NASICON-type $Li_{1.3}Al_{0.3}Ti_{1.7}(PO_4)_3$ [39,40]. This process is less straightforward during the second cycle. In this respect, the use of a composite electrode may result in difficulties to detect the reversible redox process due to Ti^{4+}/Ti^{3+} couple, according to the literature [38]. This redox reaction may limit the practical operational voltage window of high-V cathodes (e.g., Li-rich layered oxide compounds, LRLO), which are usually discharged down to 2.5 V vs. Li^+/Li. At the same time, on the anode side, the use of a polymer electrolyte devoid of the NASICON-type conductor, preferably in a multi-layered assembly, is envisaged [41,42]. Anyway, increasing the amount of sintering additives could be a viable strategy to hinder electronic conduction and lithium uptake [39]. At lower potentials, other signals are observed in the CV with both the composite electrodes. According to the literature, the lithiation of amorphous Ge during the CV of a Li metal cell results in multiple peaks at approximately 0.53, 0.33, and 0.13 V [34]. In another report, the CV analyses of Li metal cells with GeO_2/C and Ge/GeO_2/C composite electrodes show reduced signals with minima at 1 and 0.7 V due to GeO_2 conversion yielding Ge + Li_2O, [42] and a broad peak near 0.1 V due to Li-Ge alloying [42]. The subsequent oxidation results in a peak at 0.4 V (Li dealloying), and broad signals with maxima at ≈1.2 and 1.7 V (reoxidation of Ge to GeO_2). These processes seem to be well reflected by the signals centred at ≈ 1, 0.6 and 0.1 V upon reduction, and the peaks with maxima at ≈ 0.4, 1 and 1.7 V upon oxidation during the first cycle in Fig. 8A and Fig. S3. In this respect, a contribution due to the presence of C65 cannot be ruled out, as emerges by comparison with the CV obtained with a CC-Cu composite electrode (inset of Fig. 8A), even though the content of C65 is considerably higher in this latter case (i.e., 90 wt.% in CC-Cu, *vs.* 15 wt.% in LAGTPB-b and LAGTP-b composites). Anyway, the sharp peak located at ≈ 0.1 V visible during the first reduction sweep with both LAGTPB-b and LAGTP-b, and the following oxidation at ≈ 0.4 and 1.7 V during the reverse scan, arise from the redox activity of Ge^{4+} in the NASICON-type structure and in GeO_2 secondary phase, as also observed with $Li_{1.5}Al_{0.5}Ge_{1.5}(PO_4)_3$ [43], or to the further reduction (and subsequent oxidation) of Ti^{3+} [44].

Fig. S4 shows the CV scans from the OCV to 5 V vs. Li QRE using LAGTPB-b and LAGTP-b composites as the WEs and LP30 as the electrolyte. The CV, using CC-Al (90 wt.% C65 carbon, 10 wt.% PVdF) as the WE, is shown for comparison purpose. It is worth noting that the scans during the second cycle are almost perfectly matched for all the samples. In contact with the CC-Al WE, LP30 probably undergoes decomposition at lower potentials compared to those reported for non-catalytically active glassy carbon [45], which might mask the signals due to the oxidation of LAGTP-b and LAGTPB-b. Therefore, this measurement is not conclusive to assess the oxidative degradation of the ceramic samples. Thus, to determine the ASW of LAGTPB-b, a multi-layered cell was prepared using a PEO-based polymer electrolyte (PEO-G4) [26] as an interlayer between the Li metal electrode and the thermally treated bulk ceramic LAGTPB-b. This method was adopted to avoid the reduction of LAGTPB-b in contact with Li metal. A gold WE was directly sputtered on LAGTPB-b, yielding a two electrodes cell in the configuration

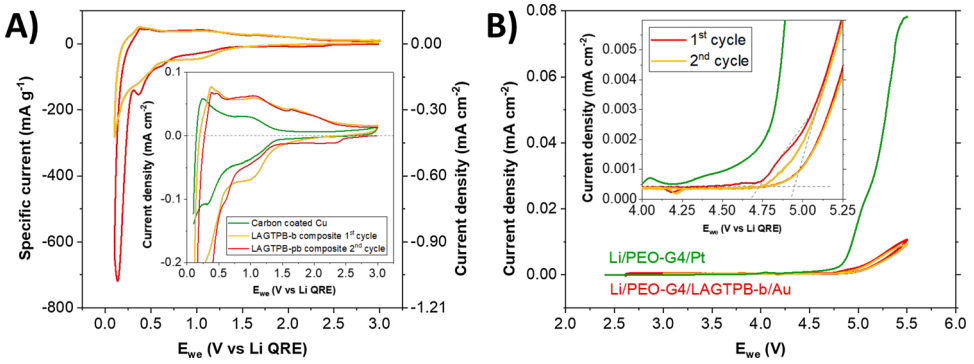

Fig. 8. CV scans at 0.1 mV s^{-1} and ambient laboratory temperature (≈ 23 °C) of three electrodes electrochemical cells cycled in cathodic/anodic potential ranges and in different configurations as follows: A) OCV – 0.1 V (cathodic), three electrode cell with Li metal CE and QRE, LiTFSI 1 m in G4 liquid electrolyte, and LAGTPB-b composite (red line 1st cycle, orange line 2nd cycle) or CC-Cu (green line) WEs, and B) OCV – 5.5 V (anodic), of a Li/PEO-G4/LAGTPB-b/Au cell (red line 1st cycle, orange line 2nd cycle) and a Li/PEO/Pt cell (one sweep, green line).

Li/PEO-G4/LAGTPB-b/Au. The Li metal foil was used as both the counter and the reference electrodes for the CV measurement up to 5.5 V at 0.1 mV s^{-1} (Fig. 8B). Under this condition, a very low (< 2 μA cm^{-2}) oxidation current starts flowing at approximately 4.75 V, followed by an exponential increase with onset at ≈ 4.95 V. These results are in fair agreement with the computed anodic stability of NASICON-type LATP, which is oxidized at 4.21 V yielding O_2, $LiTi_2(PO_4)_3$, $Li_4P_2O_7$, $AlPO_4$ as equilibrium phases, and fully delithiated above 5 V vs. Li^+/Li, according to the literature [44]. The oxidation of the polymer electrolyte is ruled out based on the comparison with the linear sweep voltammetry scan at 0.1 mV s^{-1} using a two electrodes cell with a Li/PEO-G4/Pt configuration, where the oxidation current starts flowing at ≈ 4 V (with a constant increase after 4.2 V) and the onset of the exponential increase of the current (due to the oxidative decomposition) is located at ≈ 4.8 V (Fig. 8B). An additional Li/PEO-G4/LAGTPB-b/Au cell was tested by CV in the range from 2 to 3 V where the signals due to Ti^{4+}/Ti^{3+} redox couple are supposed to be located (**Fig. S5**). In the bulk form, differently from the case of the composite WE in Fig. 8A, the peaks due to Ti^{4+} reduction and Ti^{3+} oxidation are clearly seen, with maxima at ≈ 2.1 and 2.6 V, respectively.

Overall, the measured oxidation stability of the highly conductive LAGTPB-b under study is high enough to allow safe charging of high-V cathodes, while the discharge voltage should be limited to prevent Ti^{4+} reduction, even though further addition of sintering agents and processing the material in the form of a composite ceramic-polymer hybrid electrolyte is envisaged to mitigate this phenomenon and will be object of future investigation.

4. Conclusions

A glass-ceramic LAGTP system with composition $Li_{1.4}Al_{0.4}Ge_{0.4}Ti_{1.4}(PO_4)_3$ was successfully prepared through a melt-casting technique and the addition of B_2O_3, commonly used for LAGP systems as a sintering aid, was investigated. The melts were casted onto a brass plate and two synthesizing routes, *viz.* powder sintering and bulk heat treatment, were followed for the as-casted materials. The effects on the resulting microstructures and ionic conductivities were investigated, together with those of B_2O_3.

Within the same composition, the bulk heat treatment led to increased grain size and cohesion, as well as to the formation of localized voids rather than widespread intergranular voids compared to the powder sintering route. On the other hand, within the same synthesizing route, the addition of B_2O_3 promoted grain growth and cohesion, and contrasted microcracks formation thanks to its ability as a sintering aid to induce grain reorganization above its melting temperature of 450 °C. Despite its addition resulted in the formation of increased amounts of secondary phases, the negative effects on ionic conductivity of these latter were however less impactful than the overall positive effects induced by its presence. In accordance with these results, the highest conductivity value of about 3.9×10^{-4} S cm^{-1} at 20 °C was recorded for bulk B_2O_3-added LAGTPB-b, with an activation energy of 0.28 eV. Ionic conductivity was seen to decrease, in agreement with the increase of the activation energy, when B_2O_3 was not introduced in the glass-ceramic composition, and further properties deterioration was observed for the powder sintered samples. The LAGTPB-b based electrolyte was found to be electrochemically stable up to about 4.8 V (vs. Li^+/Li°), making it appealing as separating electrolyte for lithium-based battery systems operating at high voltages.

Overall, the improved performance of bulk materials compared to their powder sintered counterpart was demonstrated, along with the positive effect of B_2O_3 addition on the microstructural and, thus, on the ion transport properties of this LAGTP system. The formation of large cohesive grains is very promising for the future dispersion of these systems into a polymer matrix, where the effect of grain boundaries on the overall ionic conductivity of the composite electrolyte would be further reduced upon milling of the bulk heat-treated materials. In this scenario, based on the promising results reported in the present work, we are now working in our laboratories on the dispersion of these LAGTP and LAGTPB glass-ceramics into a polymer matrix for the fabrication of composite polymer electrolytes. Therefore, conclusions will be drawn also considering the specific application and peculiarity.

Declaration of Competing Interest

The authors declare that they have no known competing financial interests or personal relationships that could have appeared to influence the work reported in this paper.

Acknowledgements

The Si-DRIVE Project (https://sidrive2020.eu/) received funding from the European Union's Horizon 2020 research and innovation program under Grant Agreement no. 814464.

Appendix A. Supplementary data

Supplementary material related to this article can be found, in the online version, at doi:https://doi.org/10.1016/j.jeurceramsoc.2021.11.014.

References

[1] C. Wang, Y. Yang, X. Liu, H. Zhong, H. Xu, Z. Xu, H. Shao, F. Ding, Suppression of Lithium dendrite formation by using LAGP-PEO (LiTFSI) composite solid electrolyte and Lithium metal anode modified by PEO (LiTFSI) in all-solid-State Lithium batteries, ACS Appl. Mater. Interfaces 9 (2017) 13694–13702, https://doi.org/10.1021/acsami.7b00336.

[2] H. Eckert, A.C. Martins, Rodrigues Ion-conducting glass-ceramics for energy-storage applications, MRS Bull. 42 (2017) 206–212, https://doi.org/10.1557/mrs.2017.30.

[3] R. DeWees, H. Wang, Synthesis and properties of NaSICON-type LATP and LAGP solid electrolytes, ChemSusChem 12 (16) (2019) 3713–3725, https://doi.org/10.1002/cssc.201900725.

[4] X. Xu, Z. Wen, Z. Gu, X. Xu, Z. Lin, Lithium ion conductive glass ceramics in the system Li1.4Al0.4(Ge1-xTix)1.6(PO4)3 (x = 0-1.0), Solid State Ion. 171 (3–4) (2004) 207–213, https://doi.org/10.1016/j.ssi.2004.05.009.

[5] K. Takada, Progress and prospective of solid-state lithium batteries, Acta Mater. 61 (3) (2013) 759–770, https://doi.org/10.1016/j.actamat.2012.10.034.

[6] A. Rossbach, F. Tietz, S. Grieshammer, Structural and transport properties of lithium-conducting NASICON materials, J. Power Sources 391 (2018) 1–9, https://doi.org/10.1016/j.jpowsour.2018.04.059.

[7] M. Hou, F. Liang, K. Chen, Y. Dai, D. Xue, Challenges and perspectives of NASICON-type solid electrolytes for all-solid-state lithium batteries, Nanotechnology 31 (13) (2020) 132003, https://doi.org/10.1088/1361-6528/ab5be7.

[8] J.L. Narváez-Semanate, A.C.M. Rodrigues, Microstructure and ionic conductivity of Li1+xAlxTi2-x(PO4)3 NASICON glass-ceramics, Solid State Ion. 181 (25–26) (2010) 1197–1204, https://doi.org/10.1016/j.ssi.2010.05.010.

[9] A. Mertens, S. Yu, N. Schön, D.C. Gunduz, H. Tempel, R. Schierholz, F. Hausen, H. Kungl, J. Granwehr, R. Eichel, Superionic bulk conductivity in Li1.3Al0.3Ti1.7(PO4)3 solid electrolyte, Solid State Ion. 309 (2017) 180–186, https://doi.org/10.1016/j.ssi.2017.07.023.

[10] J. Fu, Superionic conductivity of glass-ceramics in the system Li_2O-Al_2O_3-TiO_2-P_2O_5, Solid State Ion. 96 (3–4) (1997) 195–200, https://doi.org/10.1016/S0167-2738(97)00018-0.

[11] J. Fu, Fast Li+ ion conducting glass-ceramics in the system Li_2O–Al_2O_3–GeO_2–P_2O_5, Solid State Ion. 104 (3–4) (1997) 191–194, https://doi.org/10.1016/S0167-2738(97)00434-7.

[12] Z. Liu, S. Venkatachalam, H. Kirchhain, L. van Wüllen, Study of the glass-to-crystal transformation of the NASICON-type solid electrolyte Li1+xAlxGe2−x (PO4), Solid State Ion. 295 (2016) 32–40, https://doi.org/10.1016/j.ssi.2016.07.006.

[13] H. Kun, W. Yanhang, Z. Chengkui, L. Yonghua, Z. Huifeng, C. Jiang, H. Bin, M. Juanrong, High-temperature X-ray analysis of phase evolution in lithium ion conductor $Li_{1.5}Al_{0.5}Ge_{1.5}(PO_4)_3$, Mater. Charact. 80 (2013) 86–91, https://doi.org/10.1016/j.matchar.2013.03.012.

[14] H. Kun, W. Yanhang, Z. Chengkui, Z. Huifeng, L. Yonghua, C. Jiang, H. Bin, M. Juanrong, Influence of Al_2O_3 additions on crystallization mechanism and conductivity of Li_2O–Ge_2O–P_2O_5 glass–ceramics, Phys. B Condens. Matter 406 (20) (2011) 3947–3950, https://doi.org/10.1016/j.physb.2011.07.033.

[15] J.S. Thokchom, B. Kumar, The effects of crystallization parameters on the ionic conductivity of a lithium aluminum germanium phosphate glass–ceramic, J. Power Sources 195 (9) (2010) 2870–2876, https://doi.org/10.1016/j.jpowsour.2009.11.037.

[16] J. Yang, Z. Huang, B. Huang, J. Zhou, X. Xu, Influence of phosphorus sources on lithium ion conducting performance in the system of Li_2O–Al_2O_3–GeO_2–P_2O_5 glass–ceramics, Solid State Ion. 270 (2015) 61–65, https://doi.org/10.1016/j.ssi.2014.12.013.

[17] P. Maldonado-Manso, E.R. Losilla, M. Martinez-Lara, M.A.G. Aranda, S. Bruque, F. E. Mouahid, M. Zahir, High Lithium ionic conductivity in the $Li_{1+x}Al_xGe_yTi_{2-x-y}(PO_4)_3$ NASICON series, Chem. Mater. 15 (9) (2003) 1879–1885, https://doi.org/10.1021/cm021717j.

[18] T. Šalkus, A. Dindune, Z. Kanepe, J. Ronis, A. Určinskas, A. Kežionis, A.F. Orliukas, Lithium ion conductors in the system $Li_{1+y}Ge_{2-x-y}Ti_xAl_y(PO_4)_3$ (x = 0.1÷0.3, y = 0.07÷0.21), Solid State Ion. 178 (21–22) (2007) 1282–1287, https://doi.org/10.1016/j.ssi.2007.07.002.

[19] P. Zhang, M. Matsui, A. Hirano, Y. Takeda, O. Yamamoto, N. Imanishi, Water-stable lithium ion conducting solid electrolyte of the $Li_{1.4}Al_{0.4}Ti_{1.6-x}Ge_x(PO_4)_3$ system (x = 0–1.0) with NASICON-type structure, Solid State Ion. 253 (2013) 175–180, https://doi.org/10.1016/j.ssi.2013.09.022.

[20] X.M. Wu, X.H. Li, Y.H. Zhang, M.F. Xu, Z.Q. He, Synthesis of $Li_{1.3}Al_{0.3}Ti_{1.7}(PO_4)_3$ by sol–gel technique, Mater. Lett. 58 (7–8) (2004) 1227–1230, https://doi.org/10.1016/j.matlet.2003.09.013.

[21] K. Waetzig, A. Rost, U. Langklotz, B. Matthey, J. Schilm, An explanation of the microcrack formation in $Li_{1.3}Al_{0.3}Ti_{1.7}(PO_4)_3$ ceramics, J. Eur. Ceram. Soc. 36 (8) (2016) 1995–2001, https://doi.org/10.1016/j.jeurceramsoc.2016.02.042.

[22] B. Tjaden, S.J. Cooper, D.J.L. Brett, D. Kramer, P.R. Shearing, On the origin and application of the Bruggeman correlation for analysing transport phenomena in electrochemical systems, Curr. Opin. Chem. Eng. 12 (2016) 44–51, https://doi.org/10.1016/j.coche.2016.02.006.

[23] A. Cordier, H. El Khal, E. Siebert, M.C. Steil, On the role of the pore morphology on the electrical conductivity of porous yttria-stabilized zirconia, J. Eur. Ceram. Soc. 39 (7) (2019) 2518–2525, https://doi.org/10.1016/j.jeurceramsoc.2019.02.027.

[24] S.D. Jackman, R.A. Cutler, Effect of microcracking on ionic conductivity in LATP, J. Power Sources 218 (2012) 65–72, https://doi.org/10.1016/j.jpowsour.2012.06.081.

[25] H.S. Jadhav, M. Cho, R.S. Kalubarme, J. Lee, K. Jung, K. Shin, C. Park, Influence of B_2O_3 addition on the ionic conductivity of $Li_{1.5}Al_{0.5}Ge_{1.5}(PO_4)_3$ glass ceramics, J. Power Sources 241 (2013) 502–508, https://doi.org/10.1016/j.jpowsour.2013.04.137.

[26] Y.-C. Kim, K.-N. Jung, J.-W. Lee, M.-S. Park, Improving the ionic conductivity of $Li_{1+x}Al_xGe_{2-x}(PO_4)_3$ solid electrolyte for all-solid-state batteries using microstructural modifiers, Ceram. Int. 46 (14) (2020) 23200–23207, https://doi.org/10.1016/j.ceramint.2020.06.101.

[27] L. Porcarelli, C. Gerbaldi, F. Bella, J.R. Nair, Super soft all-ethylene oxide polymer electrolyte for safe all-solid lithium batteries, Sci. Rep. 6 (1) (2016) 1–14, https://doi.org/10.1038/srep19892.

[28] W. Soppe, C. Van Der Marel, W.F. Van Gunsteren, H.W. Den Hartog, New insights into the structure of B_2O_3 glass, J. Non. Solids 103 (2–3) (1988) 201–209, https://doi.org/10.1016/0022-3093(88)90199-8.

[29] M. Illbeigi, A. Fazlali, M. Kazazi, A.H. Mohammadi, Effect of simultaneous addition of aluminum and chromium on the lithium ionic conductivity of $LiGe_2(PO_4)_3$ NASICON-type glass–ceramics, Solid State Ion. 289 (2016) 180–187, https://doi.org/10.1016/j.ssi.2016.03.012.

[30] N. Kyono, F. Bai, H. Nemori, H. Minami, D. Mori, Y. Takeda, O. Yamamoto, N. Imanishi, Lithium-ion conducting solid electrolytes of $Li_{1.4}Al_{0.4}Ge_{0.2}Ti_{1.4}(PO_4)_3$ and MO_x (M = Al, Ti, and Zr) composites, Solid State Ion. 324 (2018) 114–127, https://doi.org/10.1016/j.ssi.2018.06.016.

[31] M. Micoulaut, L. Cormier, G.S. Henderson, The structure of amorphous, crystalline and liquid GeO_2, J. Phys. Condens. Matter 18 (45) (2006) R753, https://doi.org/10.1088/0953-8984/18/45/R01.

[32] D. Balitsky, E. Philippot, V. Balitsky, L. Balitskaya, T. Setkova, T. Bublikova, P. Papet, $GaPO_4$ Single Crystals: Growth Condition by Hydrothermal Refluxing Method, Molecules 25 (19) (2020) 4518, https://doi.org/10.3390/molecules25194518.

[33] S. Duluard, A. Paillassa, P. Lenormand, P. Taberna, P. Simon, P. Rozier, F. Ansart, Dense on porous solid LATP electrolyte system: preparation and conductivity measurement, J. Am. Ceram. Soc. 100 (1) (2017) 141–149, https://doi.org/10.1111/jace.14451.

[34] G.-T. Kim, T. Kennedy, M. Brandon, H. Geaney, K.M. Ryan, S. Passerini, G. B. Appetecchi, Behavior of germanium and silicon nanowire anodes with ionic liquid electrolytes, ACS Nano 11 (6) (2017) 5933–5943, https://doi.org/10.1021/acsnano.7b01705.

[35] S. Brutti, E. Simonetti, M. De Francesco, A. Sarra, A. Paolone, O. Palumbo, S. Fantini, R. Lin, A. Falgayrat, H. Choi, M. Kuenzel, S. Passerini, G.B. Appetecchi, Ionic liquid electrolytes for high-voltage, lithium-ion batteries, J. Power Sources 479 (2020) 228791, https://doi.org/10.1016/j.jpowsour.2020.228791.

[36] Y. Xiao, Y. Wang, S.-H. Bo, J.C. Kim, L.J. Miara, G. Ceder, Understanding interface stability in solid-state batteries, Nat. Rev. Mater. 5 (2) (2020) 105–126, https://doi.org/10.1038/s41578-019-0157-5.

[37] M.S. Park, S.B. Ma, D.J. Lee, D. Im, S.-G. Doo, O. Yamamoto, A highly reversible lithium metal anode, Sci. Rep. 4 (1) (2014) 1–8, https://doi.org/10.1038/srep03815.

[38] J. Qian, W.A. Henderson, W. Xu, P. Bhattacharya, M. Engelhard3, O. Borodin, J. Zhang, High rate and stable cycling of lithium metal anode, Nat. Commun. 6 (1) (2015) 1–9, https://doi.org/10.1038/ncomms7362.

[39] P. Birke, F. Salam, S. Döring, W. Weppner, A first approach to a monolithic all solid state inorganic lithium battery, Solid State Ion. 118 (1–2) (1999) 149–157, https://doi.org/10.1016/S01672738(98)00462-7.

[40] W. Zhou, Z. Wang, Y. Pu, Y. Li, S. Xin, X. Li, J. Chen, J.B. Goodenough, Double-layer polymer electrolyte for high-voltage all-solid-state rechargeable batteries, Adv. Mater. 31 (4) (2019) 1805574, https://doi.org/10.1002/adma.201805574.

[41] M. Falco, S. Palumbo, G. Lingua, L. Silvestri, M. Winter, R. Lin, V. Pellegrini, F. Bonaccorso, J.R. Nair, C. Gerbaldi, A bilayer polymer electrolyte encompassing pyrrolidinium-based RTIL for binder-free silicon few-layer graphene nanocomposite anodes for Li-ion battery, Electrochem. commun. 118 (2020) 106807, https://doi.org/10.1016/j.elecom.2020.106807.

[42] J. Hwang, C. Jo, M.G. Kim, J. Chun, E. Lim, S. Kim, S. Jeong, Y. Kim, J. Lee, Mesoporous Ge/GeO_2/carbon lithium-ion battery anodes with high capacity and high reversibility, ACS Nano 9 (5) (2015) 5299–5309, https://doi.org/10.1021/acsnano.5b00817.

[43] J.K. Feng, L. Lu, M.O. Lai, Lithium storage capability of lithium ion conductor $Li_{1.5}Al_{0.5}Ge_{1.5}(PO_4)_3$, J. Alloys. Compd. 501 (2) (2010) 255–258, https://doi.org/10.1016/j.jallcom.2010.04.084.

[44] Y. Zhu, X. He, Y. Mo, Origin of outstanding stability in the lithium solid electrolyte materials: insights from thermodynamic analyses based on first-principles calculations, ACS Appl. Mater. Interfaces 7 (42) (2015) 23685–23693, https://doi.org/10.1021/acsami.5b07517.

[45] I. Azcarate, W. Yin, C. Méthivier, F. Ribot, C. Laberty-Robert, A. Grimaud, Assessing the oxidation behavior of EC :DMC based electrolyte on non-catalytically active surface assessing the oxidation behavior of EC :DMC based electrolyte on non-catalytically active surface, J. Electrochem. Soc. 167 (8) (2020) 080530, https://doi.org/10.1149/1945-7111/ab8f57.

[46] W. Xiao, J. Wang, L. Fan, J. Zhang, X. Li, Recent Advances in Li1+xAlxTi2-x(PO4)3 solid-state electrolyte for safe lithium batteries, Enrgy Stor. Mater. 19 (2019) 379–400, https://doi.org/10.1016/j.ensm.2018.10.012.